Journal of Alloys and Compounds 509 (2011) 9826–9835

Contents lists available at ScienceDirect

Journal of Alloys and Compounds

journal homepage: www.elsevier.com/locate/jallcom

Identification of microstructural mechanisms during densification of a TiAl alloy by spark plasma sintering

Houria Jabbar[a,b], Alain Couret[a,b], Lise Durand[a,b], Jean-Philippe Monchoux[a,b,*]

[a] CNRS, CEMES-UPR 8011 (Centre d'Elaboration de Matériaux et d'Etudes Structurales), BP 94347, 29 rue J. Marvig, F-31055 Toulouse, France
[b] Université de Toulouse, UPS, F-31055 Toulouse, France

ARTICLE INFO

Article history:
Received 4 July 2011
Received in revised form 29 July 2011
Accepted 2 August 2011
Available online 10 August 2011

Keywords:
Intermetallics
Titanium aluminides
Powder metallurgy
Precipitation
Plastic deformation
Electron microscopy

ABSTRACT

This work aims at identifying, by coupled scanning and transmission electron microscopy (SEM and TEM) observations, the densification mechanisms occurring when an atomized Ti–47Al–1W–1Re–0.2Si powder is densified by spark plasma sintering (SPS). For this purpose, interruptions of the SPS cycle have been performed to follow the evolution of the microstructure step by step. The powder particles exhibit a classical dendritic microstructure containing a large amount of out-of-equilibrium α phase. During heating-up, the microstructure undergoes successive transformations. At T = 525–875 °C the α phase transforms into γ. The γ phase formed is supersaturated in W and Re. It de-saturates for T above 875 °C by discontinuous precipitation of W and Re-rich B2 phase. Densification takes place for T between 900 °C and 1150 °C by plastic deformation of the powder particles. TEM observations show that the repartition of the plastic deformation is correlated to the dendritic microstructure, and that dynamic recrystallization mechanisms occur. Microstructural phenomena directly resulting from the high currents involved in the SPS process have not been observed.

1. Introduction

The sintering technique known as spark plasma sintering (SPS) has been the subject of intense developments in the past decade [1,2] because of its astonishing performances. With this technique, sintering rates 10–100 times faster than that of the classical sintering techniques are currently achieved. The principle of the SPS is to submit a powder to electric current pulses of high intensity with simultaneous application of a uniaxial pressure. However, despite the strong technological interest for this technique, very little studies focus on the understanding of the underlying mechanisms involved. Hence, our aim is to give an insight into the metallurgical mechanisms that take place during sintering by SPS of an intermetallic alloy, the G4 TiAl alloy.

The TiAl alloys are interesting for applications as turbine blades of aircraft reactors because of their elevated mechanical resistance at high temperatures combined with a low density of the material. An alloy has been developed by the General Electric company (GE alloy) and has been installed into aircraft engines. First attempts to process GE alloys by SPS have been highly promising, since materials exhibiting high room temperature strength and ductility with good repeatability have been obtained [3,4]. These results lead us to further develop this technique to Nb-containing TiAl alloys specifically designed for creep resistance [5]. From these studies, the necessity to understand the metallurgical mechanisms taking place during elaboration by SPS arose, in order to better understand the resulting microstructures and their mechanical properties. For this purpose, we chose to work with the G4 alloy, because this alloy is particularly interesting in reason of its good compromise between tensile and creep properties [6]. We present here a study of the evolution of the microstructure of the alloy during sintering, by performing interrupted tests of the SPS process and by carrying out coupled transmission electron microscopy (TEM) and scanning transmission microscopy (SEM) observations.

2. Experimental

G4 powder of composition Ti–47Al–1W–1Re–0.2Si and 50–200 μm granulometry provided by ONERA and atomized by GKSS by the plasma melting induction guiding gas atomization process [7] has been employed. In this process, the cooling rate of the powder particles is extremely fast (of the order of 10^4–10^5 K/m), favoring stabilization of a large amount of metastable α phase at the end of atomization [7].

The SPS processing procedure for TiAl alloys has been described in Refs. [4,5,8]. The Sumitomo 2080 SPS machine of the "Plateforme Nationale de Frittage Flash du CNRS, Toulouse" has been used. Dies 8 mm in diameter have been employed. Because there is an intense heat loss by radiation from the external surfaces of the dies, a thermal gradient is established from the samples to the surface of the dies [1,2,8]. This implies that the temperature measured by the pyrometer, T_{SPS} is different from that of the sample, T. For 8 mm dies, these temperatures are linked by: $T = T_{SPS} + 25$ °C [8]. All temperatures given in this paper are sample temperatures (T) except otherwise stated.

---

* Corresponding author at: CNRS, CEMES-UPR 8011 (Centre d'Elaboration de Matériaux et d'Etudes Structurales), BP 94347, 29 rue J. Marvig, F-31055 Toulouse, France. Tel.: +33 5 62 25 79 79; fax: +33 5 62 25 79 99.
E-mail address: monchoux@cemes.fr (J.-P. Monchoux).

0925-8388/$ – see front matter © 2011 Elsevier B.V. All rights reserved.
doi:10.1016/j.jallcom.2011.08.008

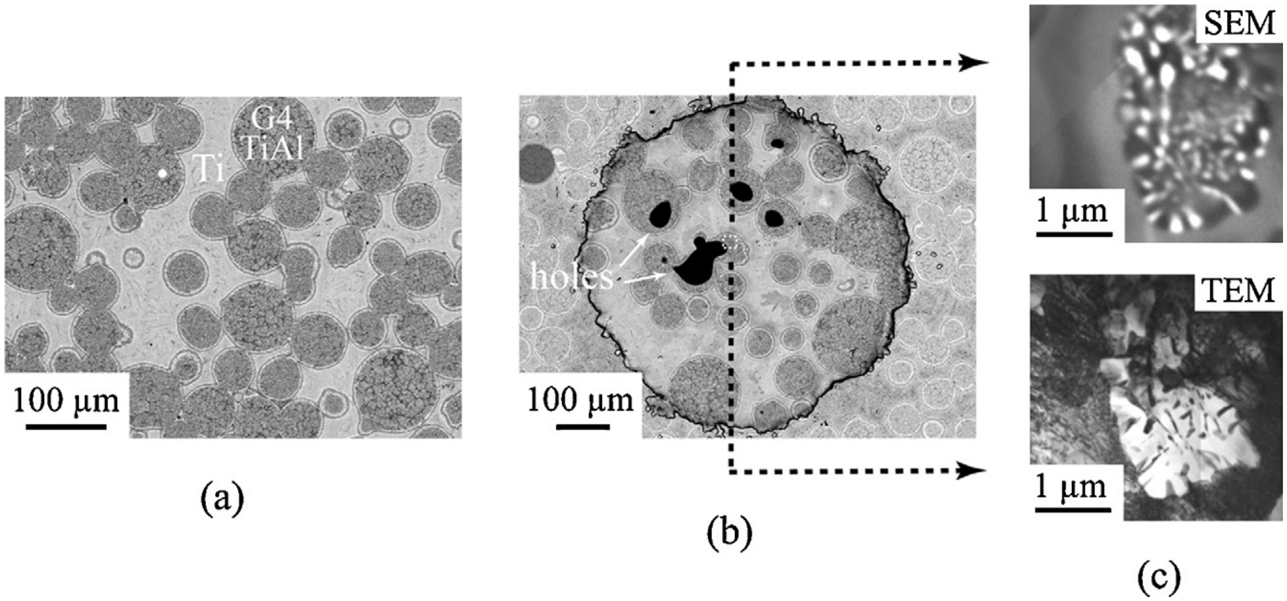

Fig. 1. G4 powder particles incorporated in Ti for metallographic observation of unconsolidated sample ($T = 975\,^{\circ}$C). (a) General view (SEM micrograph). Ti–TiAl interdiffusion zones appear as white lines around the TiAl powder particles. (b) SEM observation of a TEM thin foil of this sample prepared by electropolishing. The electropolished region is seen as the large circular region occupying most of the micrograph. In this region, holes can be seen, at the edge of which TEM observations are made. (c) SEM micrograph of a region close to the edge of a hole, and TEM observation of the same region.

An analysis of a complete sintering cycle will be given later. During this cycle, interruptions of the sintering process have been performed to study the evolution of the microstructure of the samples at the corresponding steps. This has been achieved by turning off the current and pressure at the desired step and by leaving the sample and matrix cool down in the vacuum of the SPS chamber at a rate measured as of the order of 500–1000 °C/min. Microstructure evolution may occur during this relatively slow cooling rate. However, we will suppose that this effect is limited. For interruptions at temperatures lower than the end of sintering ($T \approx 1150\,^{\circ}$C, see next section), the sample was too porous to give a consolidated sample suitable for metallographic preparation. Then, for microstructure observations at temperatures below $T \approx 1150\,^{\circ}$C, we have mixed G4 powder particles with metallic powders which sinter at low temperature. For this purpose, Al was employed at 525 °C, and Ti at 875 °C and 975 °C. Fig. 1a gives an example of incorporation of G4 particles into Ti ($T = 975\,^{\circ}$C). The TiAl powder particles are seen in dark grey. They are immerged in a Ti matrix appearing in light grey. There is a zone of interdiffusion between Ti and TiAl at the periphery of the particles, but its extension is limited. Care was taken to perform observations away of this zone.

Sample preparation for SEM and TEM have been performed using standard procedures for TiAl alloys [5]. Samples consisting of G4 powder sintered with Al or Ti have been prepared by a Gatan precision ion polishing system (PIPS). For this purpose, the final mechanical grinding procedure was performed using a tripode, to thin the sample down to about 10 µm. The ion milling angle was set to 7°. At the beginning, the ion energy was 6 keV then it was reduced to 3 keV once a hole was formed, to remove the irradiation damaged layer formed by the 6 keV beam.

SEM observations have been performed with a Jeol 6490 SEM equipped with the Oxford Inca energy dispersive spectroscopy (EDS) system. TEM observations have been carried out with a Jeol 2010 TEM. Coupled SEM–TEM observations of the same zones of samples have been performed in some cases, by observing TEM thin foils by SEM (see an example in Fig. 1b and c). The correspondence of the SEM and TEM micrographs allowed localizing accurately the observed zones. This also allowed avoiding observation of the Ti–TiAl interdiffusion zone around the TiAl powder particles. EDS analyzes in STEM mode have been performed with a FEI CM20 Feg TEM equipped with a Bruker EDS system, to obtain chemical information at a finer scale than with a SEM. EBSD analyses have been performed using a Jeol JSM 6500F SEM. The X-ray analyses have been performed with a Seifert XRD3000P diffractometer using Cu-K_{α} radiation. The diffractograms have been recorded between 20° and 70° with an acquisition time of 16 s per step each 0.02°. Qualitative volume fractions estimated from X-ray peak intensities have been estimated using the Powdercell software [9].

3. Results

3.1. Analysis of the SPS cycle

Fig. 2 gives records of punch displacement d, pressure P and SPS temperature T_{SPS} (recall that SPS and sample temperatures are linked by: $T = T_{SPS} + 25\,^{\circ}$C) in a typical experiment. We give here the main features of this cycle. The temperature ramp was set to 100 °C/min, then reduced to 25 °C slightly below the plateau temperature to avoid excessive overshooting of the desired temperature. Although the contribution of the thermal expansion has not been accounted for and subtracted from the recorded values, densification can be approximately deduced from the variation of d. Then, densification occurs between $t \approx 6$ min and 9 min, that is, between $T \approx 900\,^{\circ}$C and 1150 °C (we do not consider the slight compaction resulting from application of the pressure between 0 and 2 min). The sintering cycle can then be schematically divided into two steps. (i) A first step during which the powder is subjected to influence of temperature only (T between room temperature and 900 °C). (ii) A second step for $T > 900\,^{\circ}$C, corresponding to densification under the influence of temperature and pressure. A precipitation phenomenon occurs around 875–975 °C, that is, at the boundary between these two domains. But because pressure has little influence on this phenomenon, it will be presented with the first step.

3.2. Characterization of the as atomized microstructure

The microstructure observed at room temperature of cast G4 alloys consists of ≈90% of γ phase, ≈10% of B2 phase (vol. fractions) [6] and slight fractions of α_2 and Ti_5Si_3 phases [6,10,11]. Due to their low fractions, the α_2 and Ti_5Si_3 phases have not been investigated in this study. Moreover, we have not systematically distinguished between the low-temperature ordered α_2 and B2 phases, and high-temperature disordered α and β phases, and we will most of the time call them (maybe abusively) α and β. In powders, due to the fast quenching rate of the liquid particles during atomization, the powder particles contain a large fraction of out of equilibrium α phase [7,12,13]. In our case, estimates of volume fractions from X-ray measurements gave: 27% of γ, 65% of α and 8% of β. Fig. 3 shows the microstructure of the powder after sintering at 525 °C, that is, very close to the as-atomized state. This microstructure corresponds to a classical dendritic microstructure, in which can be identified by comparison with microstructures of cast G4 alloys [6]: dendritic arms (DA), interdendritic channels (IC) and skeletons

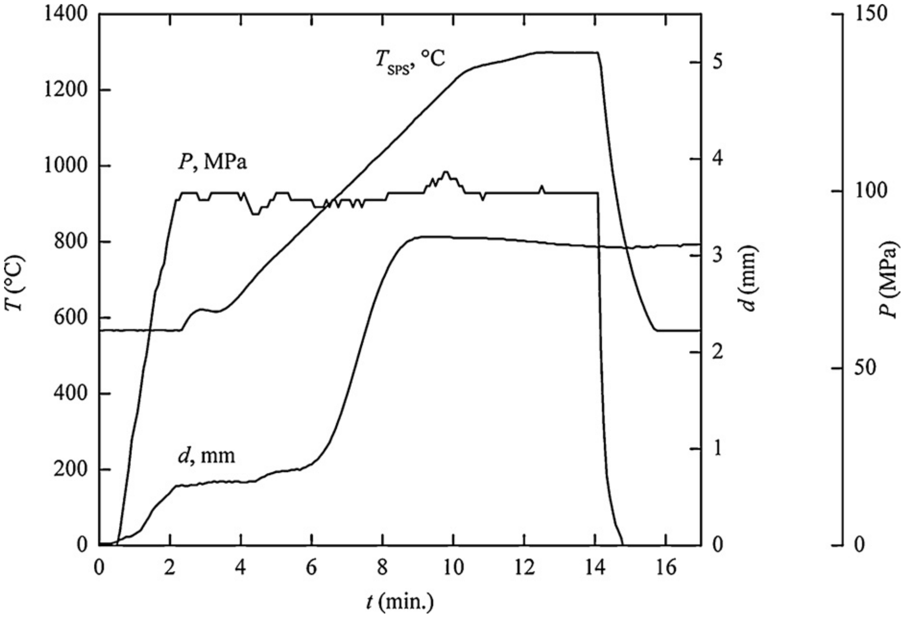

Fig. 2. Example of records of SPS parameters for a typical experiment: SPS temperature (T_{SPS}, °C), pressure (P, MPa) and punch displacement (d, mm, defined as positive when the punches approach from each other).

of B2 phase at the center of the DA. The dendrites correspond to primary β phase which nucleated in the liquid and transformed at lower temperature into α. The IC result from peritectic solidification of the remaining liquid into α which transformed at lower temperature into γ. The B2 skeleton results from retention of β phase. EBSD analyzes (Fig. 3d and e) shows that the α and γ grain size is of the order of 20 μm. Concerning partition of W and Re between the β, α and γ phases, literature analysis shows that the solubilities range as follows: $C_W^\beta > C_W^\alpha > C_W^\gamma$ and $C_{Re}^\beta \approx C_{Re}^\alpha > C_{Re}^\gamma$ [6,14–18]. EDS mappings (Fig. 3b and c) show that W is more concentrated in the DA than in the IC. Re exhibits the same behavior, but less pronounced. This was confirmed by more accurate EDS point analyses (not shown). It has also been shown that the W and (to a lesser extent) Re concentrations in the DA decrease from the B2 skeleton to the periphery of the dendrites. The bright contrast of the DA in BSE results then from their high concentration in W and, to a lesser extent, Re. Last, Fig. 4 shows the dendritic structures of particles of ≈50 μm and ≈150 μm in diameter (referred to as small and large

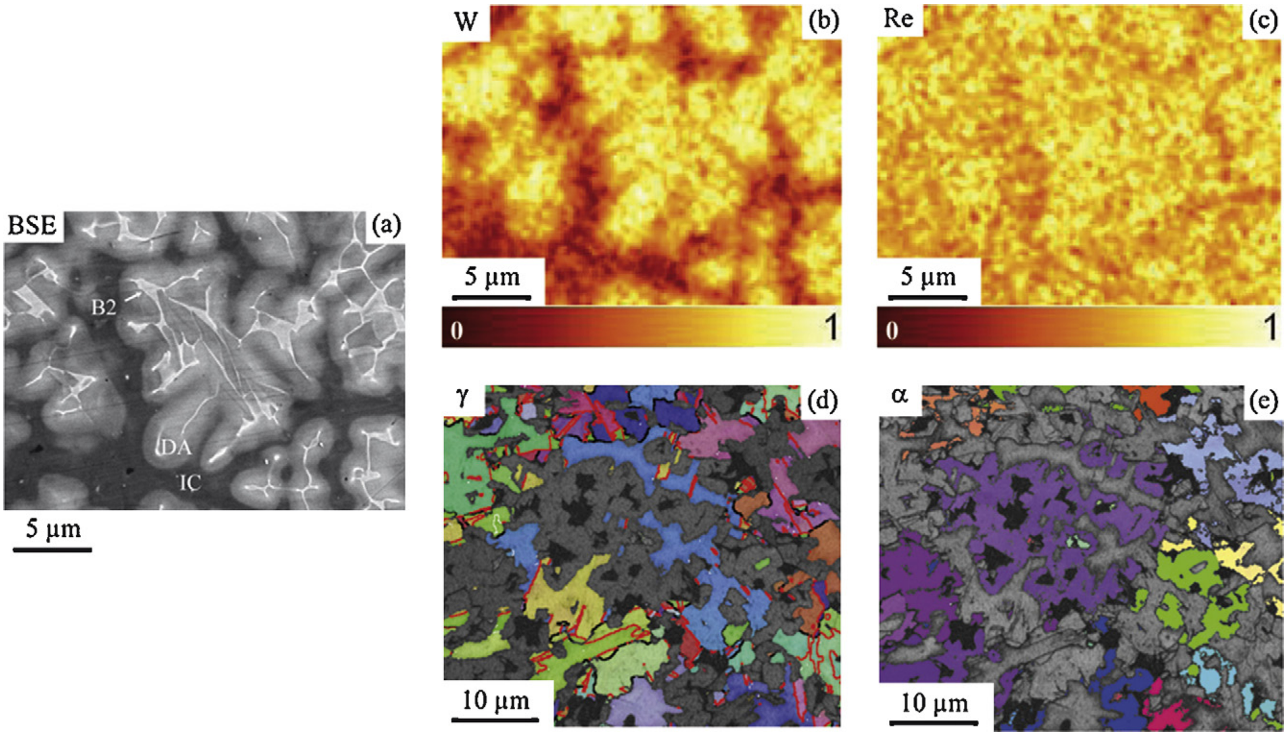

Fig. 3. (a) Micrograph of the microstructure at 525 °C (SEM BSE), with corresponding EDS chemical maps of W (b) and Re (c) (the scale below the EDS mappings gives rough indication of the concentration in at.%). Examples of DA (light grey), IC (dark grey) and B2 skeleton (white) are indicated in image (a). (d and e) SEM-EBSD orientation maps of the γ (d) and α (e) phases of another zone of the same sample. Each color represents a given crystallographic orientation.

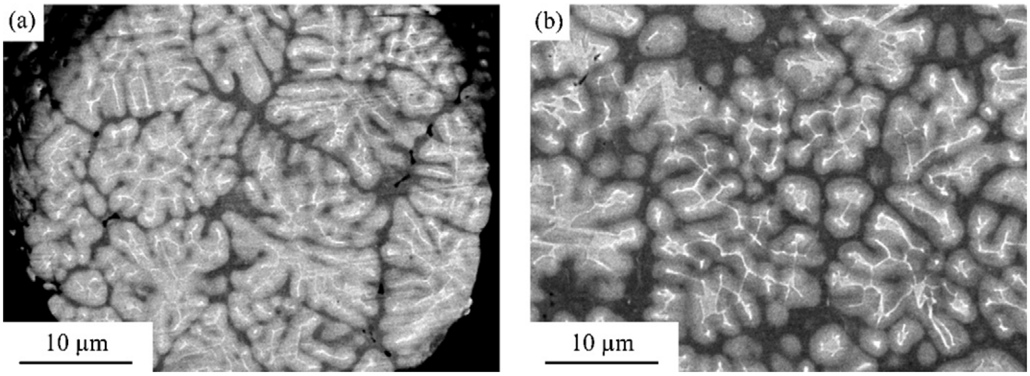

Fig. 4. Dendritic structures of small (a) and large (b) particles (SEM BSE micrographs at the same magnification).

particles, respectively). In both cases, the sizes of the whole dendrites are about the same, but the DA and the IC are thinner in the small particles with respect to the large ones. These differences are attributed to differences in quenching rates between the small and large particles [7,13].

3.3. First step: microstructure evolution under influence of T

X-ray analyzes show that during heating, the out of equilibrium α phase irreversibly transforms into γ, as already shown in Ref. [13]. At 875 °C, volume fractions estimated from X-ray analyzes are as follows: 87% of γ, 9% of α and 4% of β. These values do not significantly evolve when temperature increases. This microstructure can then be described as constituted of γ phase containing slight fractions of α and β phases. Fig. 5a shows this microstructure. The BSE contrast shows that W and Re are still concentrated in the DA and have then not been homogenized. The DA are then constituted of γ phase supersaturated in W and Re (γ_{ss}), and the IC are constituted of γ phase closer to equilibrium concentration in W and Re (γ_{eq}), as will be explained later.

At 975 °C, zones containing white dots develop around the B2 skeleton (Figs. 5b and 6). These observations can be readily interpreted as formation of a precipitation zone (called PZ in what follows), which begins to form close to the B2 skeleton and progressively invades the entire dendrite. The matrix in the PZ appears with a darker contrast than the matrix outside the PZ. This can be associated with a lower concentration in W and Re in the PZ with respect to the surrounding dendritic matrix, resulting from segregation of W and Re in the B2 precipitates. Fig. 6e and f gives EDS mappings of W and Re in the region of the PZ2, which confirm that the γ_{eq} phase is poorer in W and Re than the γ_{ss} phase, and that the concentration in W and Re is discontinuous at this interface. Besides, the BSE micrographs (Fig. 6a) indicate that there is qualitatively a lower difference in Re composition between the IC and the DA than for W.

Closer examination of the B2 precipitates morphology attached at the γ_{ss}–γ_{eq} interface shows that they are often elongated in the direction perpendicular to this interface (Fig. 6d, arrows). The regions between the PZ, which are then constituted of IC and of the remaining zone of the DA in which the precipitation phenomenon has not taken place, will be referred to as IC + DA zones. TEM observations show that the grain size of the PZ is about 0.5–1 μm (Fig. 6b and c). Dark field and selected area diffraction experiments (not shown here) have indicated that the IC + DA region is constituted of single grains larger than 10 μm. This is coherent with the EBSD analyses, which have shown that the initial size of the dendritic and interdendritic grains was about 20 μm (Fig. 3d and e). Then, the process of precipitation is accompanied by fragmentation of the large dendritic grains (about 20 μm) into smaller grains (about 0.5–1 μm) in the PZ.

Finally, the B2 initial skeleton which is visible as continuous white lines at 875 °C (Fig. 5a), is no more visible at some places at 975 °C (Figs. 5b and 6a). It has then been fragmented into individual B2 globular precipitates. Consequently, it is sometime difficult to say when considering a given precipitate if it comes from W precipitation or from breaking up of the B2 skeleton.

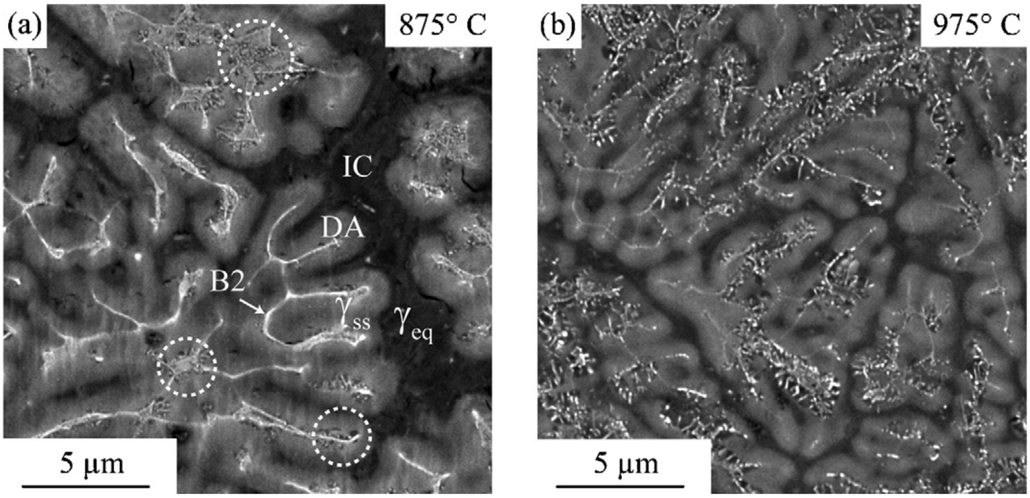

Fig. 5. (a) Microstructure after annealing at 875 °C. The DA are constituted of γ_{ss} and the IC are constituted of γ_{eq}. Some zones containing white dots in the vicinity of the B2 skeleton are circled. (b) Microstructure after annealing at 975 °C. Zones constituted by white dots in a darker matrix at the center of the DA are visible.

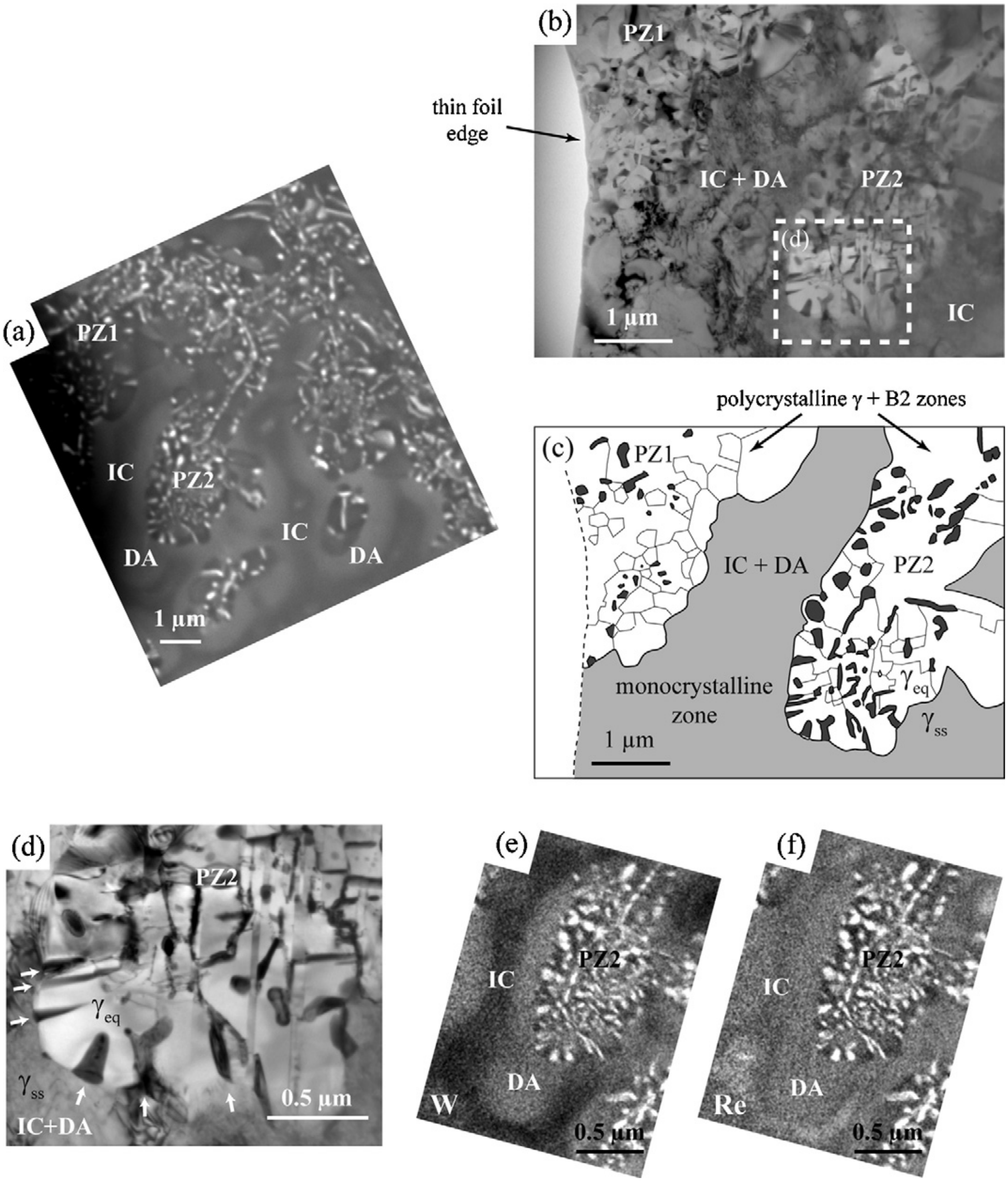

Fig. 6. (a) Microstructure at 975 °C observed by SEM, showing precipitation zones (PZ), dendritic arms (DA) in light grey and interdendritic channels (IC) in dark grey. (b) TEM micrograph of part of the same zone as image (a). By comparison with image (a), PZ and IC can be identified, but DA are not visible and cannot be accurately delimited. Two precipitation zones have been labeled PZ1 and PZ2 for clear locating on the SEM and TEM images. (c) Schematic drawing of micrograph (b) with some of the B2 precipitates (dark grey) and grain boundaries (thin lines) represented. (d) Higher magnification TEM micrograph of the zone delimited in micrograph (b). At the interface between the PZ and the IC + DA zone (γ_{ss}–γ_{eq} interface), the B2 precipitates in dark grey are oriented perpendicular to this interface (arrows). (e and f) EDS mapping by TEM of W and Re, respectively, of the PZ2 region (grey level proportional to mass fraction).

A closer examination of Fig. 5a shows that the precipitation has already begun at 875 °C (some examples are encircled in Fig. 5a).

3.4. Second step: microstructure evolution under influence of P + T

When T increases above 900 °C, densification starts under action of the applied pressure P. Fig. 7 shows micrographs of a sample after interruption of sintering at 1025 °C and polished parallel to the axis of compression. At this temperature, densification has started but is not complete, and many large voids are visible. Fig. 7b shows that some of the particles are strongly deformed. Thus, densification can be readily associated with the observed plastic deformation of the particles. Note that the degree of deformation is not the same for all the particles. Some are intensively deformed (see *e.g.* the particle in the center of Fig. 7b), whereas other are almost not deformed (see *e.g.* the particle in the center of Fig. 7a). The dendritic structure of the most deformed particles exhibits thin DA and IC, and corresponds then to small particles as shown in Fig. 4. The large particles are only little deformed.

When large particles are in contact and are forced to deform (Fig. 8), the dendritic microstructure is perturbed in the regions close to the boundaries between adjacent particles. This shows that in this case, the deformation state is the highest at the periphery of the particles. Fig. 8 shows also that the contact zones between adjacent particles exhibit geometrical singularities characterized by null values of the radius of curvature ($a = 0$, see Fig. 8d). This observation rules out matter transport mechanisms (surface, grain boundary and volume diffusion, evaporation-condensation) as dominant mechanisms for densification, because these mechanisms are driven by Gibbs–Thomson driving forces [19], which lead to augmentation of curvature radii and hence elimination

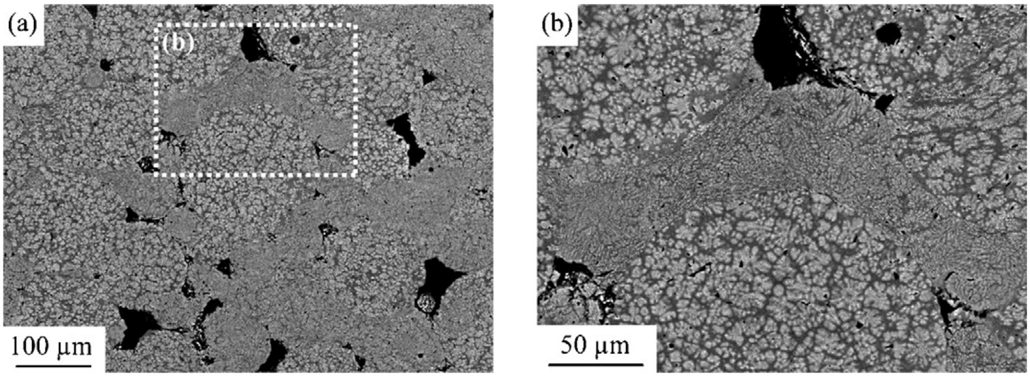

Fig. 7. SEM BSE micrograph of a sample polished parallel to the compression axis, in order to evidence the plastic deformation of the powder particles ($T = 1025\,^\circ$C, compression axis in the vertical direction). (a) General view. (b) Zoom on the zone delimited in (a).

of geometrical singularities ($a \neq 0$). In this case, a neck would grow between two adjacent particles, as schematically shown in Fig. 8e.

When temperature reaches 1150 °C, densification is complete. The deformation state of regions corresponding to small and large particles of the granulometric distribution has been studied. These regions have first been identified by low magnification SEM observations (Fig. 9a and e), then observed by SEM and TEM at higher magnifications (Fig. 9b–d and f–h). In the regions corresponding to the large particles (Fig. 9a–d), zones containing precipitates and zones free of precipitates can be clearly distinguished. They respectively correspond to the PZ and IC + DA zones resulting from the discontinuous precipitation phenomenon. An appreciable amount of dislocations can be seen in the IC + DA zones (Fig. 9c). The dislocations tend to rearrange into walls, as in classical recovery mechanisms. On the contrary, the PZ appear most of the time with a clean contrast (Fig. 9d). Thus, these zones exhibited low or very little deformation. In the small particles (Fig. 9e–h), a clear distinction between the PZ and the IC + DA zones is somewhat difficult. However, it seems from Fig. 9g and h that the same trend as in the large particles can be observed: the PZ are free of dislocations, some deformation being visible in the IC + DA zones. But globally, the small particles appear only little deformed. This apparent low deformation of the small particles is surprising, because these particles exhibit higher macroscopic deformation than the large particles. At least 5 PZ and IC + DA zones have been observed

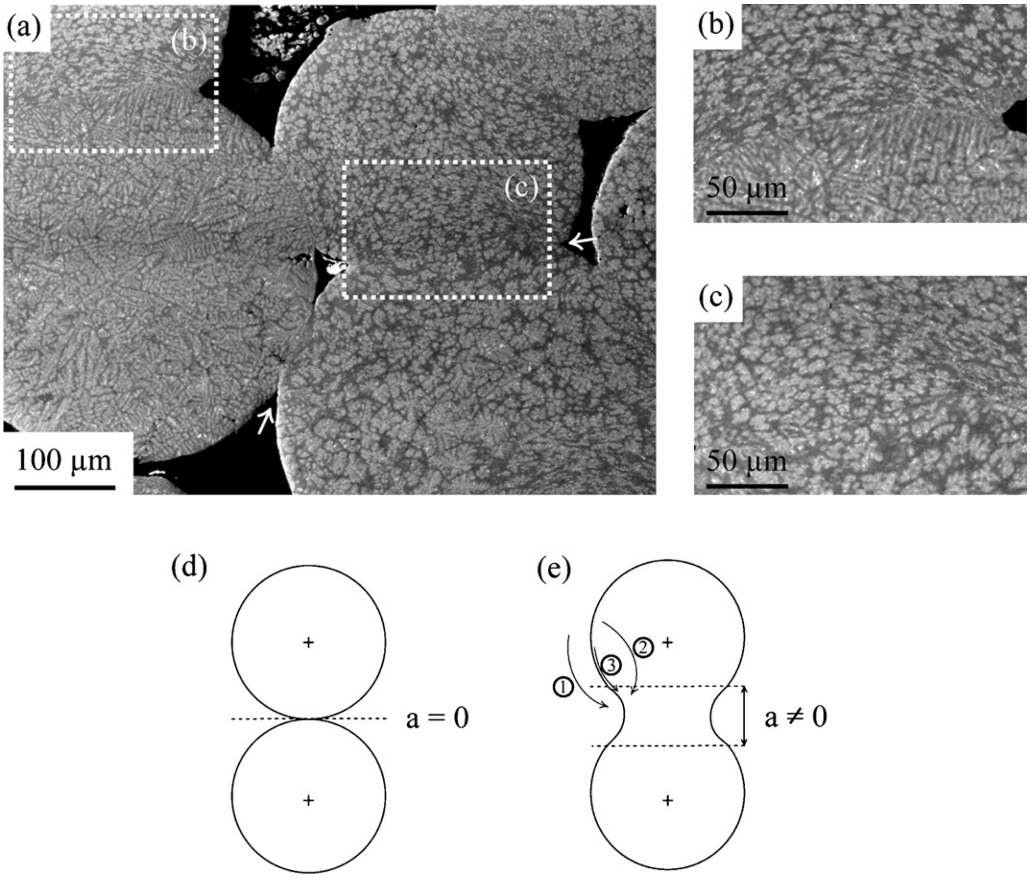

Fig. 8. (a) Large powder particles during densification ($T = 1075\,^\circ$C). Geometrical singularities (null values of curvature radius) are visible at the contact zone between particles (arrows). (b and c) Higher magnification micrographs of the zones indicated by dotted rectangles in micrograph (a), showing perturbations of the dendritic microstructure resulting from localized intense plastic deformation. (d and e) Schematic representations of the morphological evolution of the neck between two contacting particles at initial stage (d), and during densification due to evaporation-condensation (1), volume diffusion (2) and surface diffusion (3) (e).

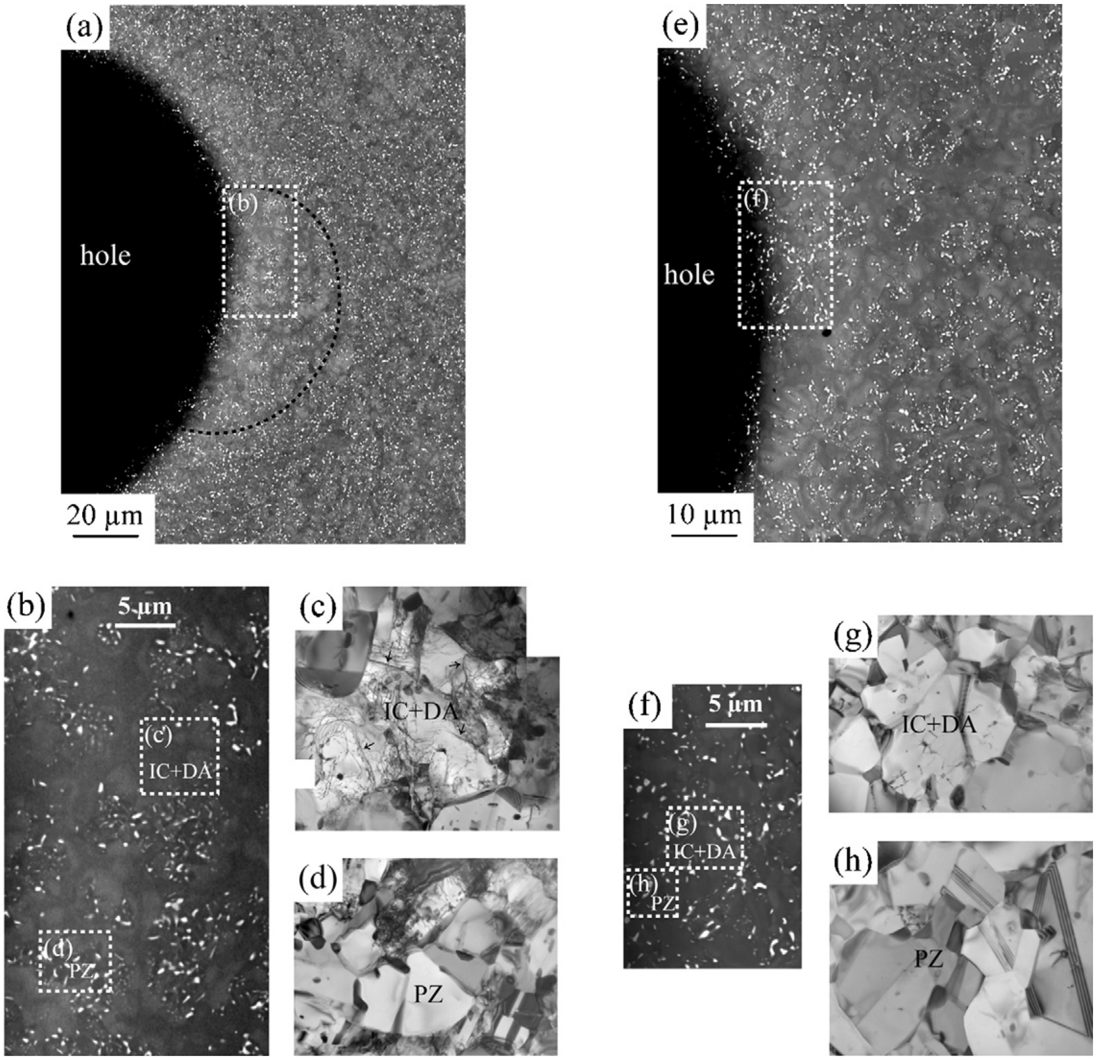

Fig. 9. SEM BSE and TEM micrographs of the microstructure at $T = 1175\,^\circ\mathrm{C}$, that is, slightly above the end of densification (1150 °C). (a and e) Low magnification SEM micrographs of two TEM thin foils of the same sample, in which regions constituted of a large particle (circled in image (a)) and of small particles (characterized by their narrow IC + DA in image (e)) can be identified. (b and f) Higher magnification SEM micrographs of the indicated zones in (a) and (e). (c and d) TEM micrographs of IC + DA and PZ of the large particle, respectively. (g and h) TEM micrographs of IC + DA and PZ of the small particle, respectively.

for small and large particles, in which the above observations have been systematically obtained [20].

Fig. 10 shows a TEM micrograph of a sample at the end of a SPS cycle ($T = 1250\,^\circ\mathrm{C}$). B2 precipitates are attached at grain boundaries. For the precipitate labeled 1, the convexity of the grain boundary indicates that this grain boundary has moved from the dislocation-free grain at the up-left of the micrograph to the grain containing dislocations at the bottom-right, as indicated by arrows in the micrograph. The radius of curvature of the interface between the precipitate and the recrystallized grain (trailing surface) is lower than that of the interface between the precipitate and the deformed grain (leading surface). This is coherent with a motion of the grain boundary in this direction, according to the Zener drag theory [21]. In other words, the dislocation-free grain grows at the expenses of the deformed grain.

4. Discussion

4.1. Initial powder microstructure

The as-atomized microstructure results from peritectic solidification, as described above. Quite coarse α and γ grains (about

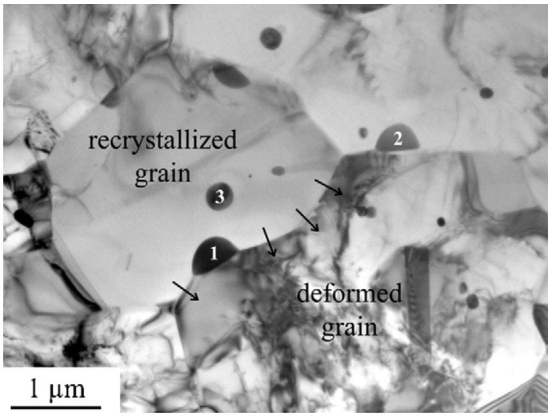

Fig. 10. TEM micrograph of a sample annealed at 1250 °C. B2 precipitates (labeled 1 and 2) are attached at grain boundaries and exhibit the classical lens shapes characteristic of a Zener drag mechanism. Another precipitate (labeled 3), not attached at a grain boundary, and thus exhibiting a quasi spherical shape, is also visible. Arrows indicate the migration direction of the grain boundary between the recrystallized and deformed grains.

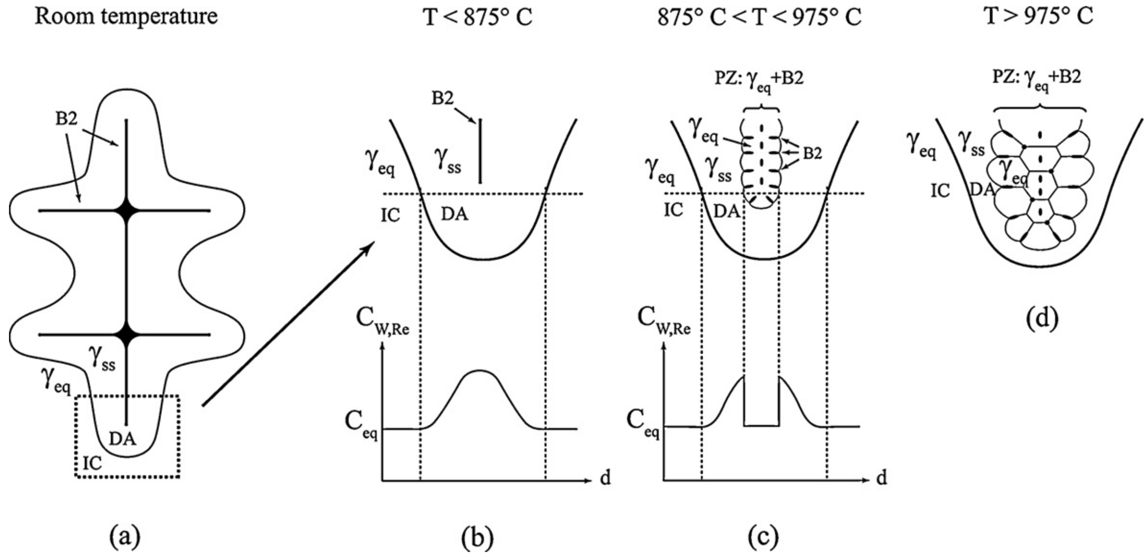

Fig. 11. Schematic representations of the discontinuous precipitation phenomenon. (a) Dendrite in the as-solidified state, constituted of γ phase supersaturated in W and Re (γ_{ss}) surrounded by γ phase closer to equilibrium (γ_{eq}). The skeleton constituted of retained B2 phase is also represented. (b–d) Evolution of the precipitation in a DA, with schematic evolution of the concentration profile in W and Re across the arm (C_{eq}: equilibrium W and Re concentration in γ_{eq}). (b) Before the onset of precipitation ($T < 875\,^\circ$C). (c) At the beginning of the development of the PZ ($875\,^\circ\text{C} < T < 975\,^\circ$C). The B2 precipitates are elongated perpendicular to the γ_{ss}–γ_{eq} interface, and the concentration in W and Re is discontinuous at this interface. Note the fragmentation of the B2 skeleton. (d) At later stage of precipitation ($T > 975\,^\circ$C). The growth of the PZ is accompanied by fragmentation of the γ_{ss} monocrystalline grain into smaller grains in the PZ.

20 μm in size), of roughly the same size as the primary β dendrites, are observed. This is surprising, because it can be expected that the existence of six different orientations for the $\beta \to \alpha$ transformation would lead to fragmentation of the initial β grain. One hypothesis to account for this observation is that nucleation of the α phase into the β is difficult, and then once a α nucleus is formed, it grows and invades entirely the β dendrite. In other words, growth would dominate over nucleation. This would also be surprising, because the fast quenching rates during the atomization process probably favor undercooling, thus favoring higher nucleation rates than growth rates. On the contrary, the oversaturation of the γ phase in W and Re can be readily associated to the fast quenching rate during atomization. As stated above, the solubility of W and Re are as follows: $C_W^\beta > C_W^\alpha > C_W^\gamma$ and $C_{Re}^\beta \approx C_{Re}^\alpha > C_{Re}^\gamma$. Then, during quenching, $\beta \to \alpha$ and $\alpha \to \gamma$ transformations occur (the latter continuing when the powder is re-heated between room temperature and 875 °C). Because these transformations occur rapidly, W and Re have not enough time to diffuse and remain "trapped" in the γ phase, thus forming γ_{ss}. The slight differences in partitioning and segregation behaviors between W and Re are also a bit unexpected, because these two elements are chemically very close. More detailed information about the role of W and Re on the transformation and phase stability of the Ti–Al system can be found in Ref. [18].

4.2. Structural transformations under the effect of temperature

As a result of the fast solidification during atomization and of the $\alpha \to \gamma$ transformation, the γ phase formed is supersaturated in W and Re, as explained above. There is then a driving force for this supersaturated γ_{ss} phase to come back towards a γ phase closer to equilibrium concentration, γ_{eq}, inducing formation of β precipitates rich in W and Re. The γ_{eq} matrix, which is depleted in W and Re as compared to the initial γ_{ss} matrix, appears then in darker contrast by BSE. The evolution of this phenomenon is schematically described in Fig. 11, based on the observations reported in Figs. 5 and 6, summarized here. The γ_{ss} matrix transforms into a PZ constituted of γ_{eq} and β precipitates, according to the reaction: $\gamma_{ss} \to \gamma_{eq} + \beta$ (Fig. 11b and c). The formed β precipitates are often attached to the γ_{ss}–γ_{eq} interface, their shape is elongated perpendicular to this interface (Fig. 11c). The concentration in W and Re $C_{W,Re}$ at this interface is discontinuous (Fig. 11c). At the same time, the initial γ_{ss} grains transform into smaller γ_{eq} grains in the PZ (Fig. 11d).

This description and the schematization given in Fig. 11, though somewhat idealized, seem to well correspond to a discontinuous precipitation mechanism. This mechanism is defined by Manna et al. [22] as a solid-state moving boundary phase transition, in which the solute composition in the matrix phases (in the reactant and product) across the migrating boundary separating these phases is discontinuous, this migrating boundary providing a short circuit path of diffusion for the solute atoms. More precisely, the discontinuous precipitation mechanism observed here corresponds to the type 1 of Williams and Butler's classification [23], because types 2 and 3 of this classification involves the presence of two reacting phases at the initial state, instead of only one phase for the type 1. This phenomenon begins close to the B2 skeleton, where the concentrations in W and Re have been shown to be the highest. Simultaneously to this discontinuous precipitation phenomenon, the β phase skeleton breaks up into globular precipitates. This probably results from classical globulization mechanisms, for which the driving force is the lowering of the free energy by reduction of the area of the interfaces [24]. At higher temperatures, the B2 precipitates grow probably by Ostwald ripening mechanisms.

4.3. Densification

For $T > 900\,^\circ$C, densification starts (Fig. 2) as a result of the plastic deformation of the powder particles (Figs. 7 and 8). The occurring of densification is rather sudden, and takes place in a short time (between about 6 min and 9 min of SPS times, see Fig. 2). It is known that in TiAl alloys, the yield stress decreases strongly above a critical temperature. For unalloyed polycrystalline TiAl, this critical temperature is about 600 °C [25]. This behavior in temperature of the TiAl alloys can account for the suddenness of densification, with a critical temperature around 900 °C in our case. We found that the small particles are considerably more deformed than the large ones. EDS analyses (not shown here) of these two classes of particles did not exhibit any significant global chemical differences between them. The dendritic morphologies between these two classes of particles (Fig. 4) are clearly different. This probably impacts their mechanical behaviors. To further explore this question, we intend to study the densification behavior of sieved powders containing only particles of small or large sizes of the granulometric distribution.

The TEM observations show how the macroscopic deformation is distributed at a more local scale. At the level of the dendritic microstructure, the deformation localizes into the interdendritic channels and dendritic arms (Fig. 9c and g), the precipitation zones remaining free of deformation (Figs. 9d and h). We interpret this observation by the fact that the new grains which form in the PZ consequently to the discontinuous precipitation phenomenon are particularly clean and free of defects (Figs. 6d and 9d, h), with respect to the surrounding IC + DA matrix (Fig. 6b and d). Then, there are no dislocation sources in the PZ to initiate deformation.

The observations show a clear tendency to recrystallization of the deformed zones. This phenomenon is more pronounced for the small particles, for which clean, deformation-free grains are visible (Fig. 9h). In the large particles, the dislocation rearrange into walls (Fig. 9c). This is characteristic of a recovery mechanism, which usually precedes recrystallization. However, the same deformation-free grains as observed in the small particles have not been observed in the large particles. It seems then that the large particles have only reached the recovery stage, and that the small particles have reached more advanced recrystallization stages. Recrystallized grains are observed at the end of densification and before any subsequent heat treatment. This shows that recrystallization occurred dynamically during densification. It can be assumed that, the higher the dislocation density, the higher is the driving force for this phenomenon. In other words, the dynamic recrystallization mechanisms would be the most advanced in the most deformed zones of the material. Then, the relatively low deformation state observed by TEM in the small particles compared to the large ones, which could appear as a paradox, can be fairly well accounted for by dynamic recrystallization mechanisms: in the small particles, the comparatively higher stored deformation energy provides a higher driving force for recrystallization than in the large particles. Zener drag mechanisms observed at higher temperature (Fig. 10) show that clean grains grow at the expenses of deformed grains. This gives another indication that recrystallization mechanisms occur. Dynamic recrystallization phenomena originating at the grain boundaries of the γ grains have previously been observed in a γ Ti–48Al–2W alloy deformed by compression at 1100–1200 °C [26,27], that is, for an alloy close to the G4 composition and for a temperature range similar to that of our observations. This is consistent with our interpretations. However, it is sometimes difficult, when observing a given clean and dislocation-free grain, to unambiguously tell whether this grain results from the discontinuous precipitation phenomenon described in Section 4.2 or from recrystallization.

The microstructure of the small particles is more affected by the microstructural evolutions discussed in this study than that of the large ones, because their initial dendritic microstructure is finer and is consequently reorganized more rapidly, and because they are also more deformed. This is the reason why the dendritic microstructure of the small particles appears almost homogenized at the end of densification (Fig. 9f). We intend to give in a next paper a thorough characterization of the microstructure of the G4 alloys at the end of the SPS process.

4.4. Effect of SPS current

A last question has to be addressed, namely, the influence of the high intensity current pulses on the sintering mechanisms. Recent reviews report on discussed electro-induced effects at the contact zones between particles [1,2]. For example, in the intermetallic FeAl alloy, cracking of oxide layer due to the SPS current accompanied by local melting at the contact zone between powder particles has been reported [28]. In our case, SEM observations (see Figs. 7 and 8) show that the microstructure of the boundaries between particles cannot be distinguished from the surrounding matrix of the two particles. TEM observations of these boundaries have been performed to look for finer features, but nothing noticeable was detected. It seems then that for micrometric powder particles, densification is dominated by the plastic deformation of the particles under the effect of the applied pressure at high temperature. Mechanisms taking place at their surfaces, as current-assisted diffusion (electromigration), cleaning of contaminated layer by plasma, cracking of oxide layer by electric discharge and local overheating at the contact zone between particles, seem then to play minor roles.

5. Conclusions

The metallurgical mechanisms occurring during sintering by SPS of a G4 Ti–47Al–1W–1Re–0.2Si alloy have been studied by coupled SEM–TEM observations of samples submitted to interrupted sintering cycles. For metallographic observations of sample in powder or porous states, dedicated experiments have been employed, based on the sintering of powder particles embedded in a metallic medium of lower sintering temperature.

The microstructure of the as-atomized G4 powder is constituted of a classical dendritic morphology resulting from peritectic solidification and contains a large amount of metastable α phase. By re-heating the powder, the metastable α phase transforms into γ phase at $T = 525–875\,^{\circ}C$. Due to rapidity of quenching during atomization, W and Re are “trapped” in the γ phase of the dendritic arms and oversaturate it. Above 875 °C, de-saturation of this γ phase occurs by the formation of precipitation zones containing B2 precipitates rich in W and Re through a discontinuous precipitation mechanism, accompanied by fragmentation of the γ grains into smaller ones. Simultaneously, globulization mechanisms induce fragmentation of the B2 skeleton.

At 900 °C, densification occurs by plastic deformation of the powder particles. The deformation principally localizes in the interdendritic channels. The precipitation zones remain largely undeformed, probably in reason of the absence of initial dislocations acting as sources for nucleation of new dislocations. The small particles are more deformed than the large ones. The analysis of the shape of the necks between the particles shows that diffusion mechanisms play minor role for densification with respect to the plastic deformation of the powder particles. No signs of other mechanisms specific to the SPS (plasma, oxide layer cracking, local overheating) are observed. At the end of densification ($T = 1175\,^{\circ}C$), recrystallization evidences are observed. Recrystallization occur then dynamically during deformation of the powder particles. This phenomenon is more advanced in the small particles than in the large ones, probably in reason of a larger amount of stored deformation energy in the former.

As a result of the mechanisms taking place during densification, the initial microstructure of the atomized powder particles is significantly transformed, in spite of the rapidity of the SPS process.

Acknowledgements

This work has been funded by a “Action inter-régionale Aquitaine & Midi-Pyrénées.” The authors whish to thank J. Crestou and D. Lamirault of the CEMES for preparation of the SEM and TEM samples. The SPS studies have been performed with the Sumitomo 2080 SPS machine of the “Plateforme Nationale de Frittage Flash du CNRS” (PNF2-CNRS, Paul Sabatier University, Toulouse, France).

References

[1] Z.A. Munir, U. Anselmi-Tamburini, M. Ohyanagi, J. Mater. Sci. 41 (2006) 763.
[2] R. Orru, R. Licheri, A.M. Locci, A. Cincotti, G. Cao, Mater. Sci. Eng. R63 (2009) 127.
[3] G. Molenat, M. Thomas, J. Galy, A. Couret, Adv. Eng. Mater. 9 (2007) 667.
[4] A. Couret, G. Molenat, J. Galy, M. Thomas, Intermetallics 16 (2008) 1134.
[5] H. Jabbar, J.P. Monchoux, F. Houdellier, M. Dollé, F.P. Schimansky, F. Pyczak, M. Thomas, A. Couret, Intermetallics 18 (2010) 2312.
[6] M. Grange, J.L. Raviart, M. Thomas, Metall. Mater. Trans. A 35A (2004) 2087.
[7] R. Gerling, H. Clemens, F.P. Schimansky, Adv. Eng. Mater. 6 (2004) 23.
[8] G. Molénat, L. Durand, J. Galy, A. Couret, J. Metall. 2010 (2010) 145431.
[9] W. Kraus, G. Nolze, J. Appl. Crystallogr. 29 (1996) 301.
[10] I. Gil, M.A. Munoz-Morris, D.G. Morris, Intermetallics 9 (2001) 373.
[11] R. Yu, L.L. He, Z.X. Jin, J.T. Guo, H.Q. Ye, Scripta Mater. 44 (2001) 911.
[12] U. Habel, C.F. Yolton, J.H. Moll, Gamma Titanium Aluminides, TMS, Warrendale, 1999.
[13] M. Charpentier, PhD Thesis, Institut National Polytechnique de Lorraine, Nancy, 2003.
[14] Y. Mizuhara, K. Hashimoto, N. Masahashi, Intermetallics 11 (2003) 807.
[15] M.A. Munoz-Morris, I. Gil, D.G. Morris, Intermetallics 13 (2005) 929.
[16] R. Kainuma, Y. Fujita, H. Mitsui, I. Ohnuma, K. Ishida, Intermetallics 8 (2000) 855.
[17] M. Thomas, J.L. Raviart, F. Popoff, Intermetallics 13 (2005) 944.
[18] C. Verstraete, PhD Thesis, Université de Paris-Sud, Orsay, 1998.
[19] Y. Adda, J. Philibert, La diffusion dans les solides – Tome I, Institut National des Sciences et Techniques Nucléaires, Saclay, 1966.
[20] H. Jabbar, PhD Thesis, Université Toulouse III Paul Sabatier, Toulouse, 2010.
[21] C.H. Hsueh, A.G. Evans, R.L. Coble, Acta Metall. 30 (1982) 1269.
[22] I. Manna, S.K. Pabi, W. Gust, Int. Mater. Rev. 46 (2001) 53.
[23] D.B. Williams, E.P. Butler, Int. Met. Rev. 26 (1981) 153.
[24] R.F. Sekerka, T.F. Marinis, Proceedings of an International Conference on Solid-solid Phase Transformations, Metallurgical Society of AIME, Pittsburgh, 1981.
[25] H.A. Lipsitt, D. Shechtman, R.E. Schafrik, Metall. Mater. Trans. A 6 (1975) 1991.
[26] H.Y. Kim, W.H. Sohn, S.H. Hong, Mater. Sci. Eng. A 251 (1998) 216.
[27] H.Y. Kim, S.H. Hong, Mater. Sci. Eng. A 271 (1999) 382.
[28] T. Grosdidier, G. Ji, F. Bernard, E. Gaffet, Z.A. Munir, S. Launois, Intermetallics 14 (2006) 1208.